

Correlation effects in magic-angle twisted bilayer graphene: An auxiliary-field quantum Monte Carlo study

Zhi-Yu Xiao

Department of Physics, College of William & Mary, Williamsburg, Virginia 23187, USA

Shiwei Zhang

Center for Computational Quantum Physics, Flatiron Institute, New York, NY 10010, USA

(Dated: June 6, 2024)

Magic angle twisted bilayer graphene (MATBG) presents a fascinating platform for investigating the effects of electron interactions in topological flat bands. The Bistritzer-MacDonald (BM) model provides a simplified quantitative description of the flat bands. Introducing long-range Coulomb interactions leads to an interacting BM (IBM) Hamiltonian, a momentum-space continuum description which offers a very natural starting point for many-body studies of MATBG. Accurate and reliable many-body computations in the IBM model are challenging, however, and have been limited mostly to special fillings, or smaller lattice sizes. We employ state-of-the-art auxiliary-field quantum Monte Carlo (AFQMC) method to study the IBM model, which constrains the sign problem to enable accurate treatment of large system sizes. We determine ground-state properties and quantify errors compared to mean-field theory calculations. Our calculations identify correlated metal states and their competition with the insulating Kramers inter-valley coherent state at both half-filling and charge neutrality. Additionally, we investigate one- and three-quarter fillings, and examine the effect of many-body corrections beyond single Slater determinant solutions. We discuss the effect that details of the IBM Hamiltonian have on the results, including different forms of double-counting corrections, and the need to establish and precisely specify many-body Hamiltonians to allow more direct and quantitative comparisons with experiments in MATBG.

I. INTRODUCTION

The interaction-driven insulating phase and superconducting phase discovered in magic-angle twisted bilayer graphene (MATBG) [1, 2] are inspiring intense efforts, in both the theoretical and experimental domains, to understand the mechanism behind them [3–19]. However, due to the interplay between electron-electron interactions and flat bands with non-trivial topology, accurate, ab initio modeling of TABLG presents many challenges [13, 14, 20–22]. The exploration of effective models for MATBG falls loosely into several categories: Hubbard-like models [5, 23] based in real-space; the so-called interacting Bistritzer and MacDonald (BM) model based in momentum space, by including long-range electron-electron interactions in the low-energy continuum BM model [3]; and more recently, a heavy fermion description [24, 25].

In this work, we take the second approach, and perform a systematic many-body study using the interacting BM (IBM) model. Previous studies of the IBM model have sought to explain the interaction-driven insulating phase with perturbation theory [13, 15] and Hartree Fock (HF) approaches [6, 13, 26–28]. Many-body studies, including exact diagonalization (ED) [15, 29], determinantal quantum Monte Carlo (DQMC) [30–33], density matrix renormalization group (DMRG) [32, 34–37] and quantum chemistry methods [38] have shown that the proper treatment of electron-electron interactions and their interplay with dispersion are indispensable for determining ground state properties. Much progress has been made in characterizing the properties of this model. Important

obstacles remain, however, for establishing comparisons and connections with experiments [1, 19, 39–43].

The obstacles are several fold. The relevant model parameters and electron fillings lie within the most difficult regime, and require very high resolution to capture accurately the interplay between band dispersion and electron-electron interactions. This is at the heart of strong correlation physics, and presents challenges of various forms to every computational method. Here the presence of topological bands and long-range interactions necessitates large system sizes in order to properly reach the thermodynamic limit. It has also become clear that the answers can be sensitive to model details including double counting corrections, the effect of remote bands, and accounting for strain, etc. The lack of accurate solutions to the model makes it more challenging to pinpoint and understand discrepancies with experimental observations.

Here we tackle this problem by employing the phaseless auxiliary-field quantum Monte Carlo (AFQMC) method [44] to investigate the ground state of the IBM model at integer fillings. Our approach is based on the momentum space description and captures the non-trivial topology by retaining eight “flat” bands. Long-range (screened) electron-electron interaction is treated explicitly and rigorously. The phaseless AFQMC method mitigates the sign/phase problem by a constrained path approximation [45, 46]; it enables simulations of large lattice sizes (here calculations are performed up to 12×12 cells), from which properties at the thermodynamic limit can be inferred. The accuracy of the constrained path approximation (more precisely the phaseless approximation [44] be-

cause of the long-range interaction) depends on the form of Hubbard-Stratonovich transformation. The particular form to decompose a long-range interaction written in momentum space has been applied in many AFQMC studies of solids [47]. A more general form to decompose a 4-index Coloumb interaction written in an arbitrary basis is also available [48, 49], and has been applied for two decades in quantum chemistry [50, 51]. The extensive benchmarks in these show that the phaseless AFQMC approach allows accurate treatment of correlated materials with long-range interactions.

Using this approach we perform a systematic and comprehensive exploration of the ground-state phase diagram of the IBM model. We focus on four integer fillings that are specified by the number of electrons per \mathbf{k} -point n_f (charge neutrality $n_f = 4$, three quarter $n_f = 3$, half-filling $n_f = 2$, and quarter-filling $n_f = 1$). Our study scans a wide range of tunneling ratio κ that captures the lattice relaxation between the intra-sublattice (AA) and inter-sublattice (AB&BA) regions.

At charge neutrality and half-filling, a transition from correlated insulating states (i.e., Kramers inter-valley coherent, K-IVC) to metallic states is observed as the tunneling ratio κ is increased. This transition is characterized by the correlation energy, charge gap, and related order parameters. Our results indicate a loss of K-IVC long-range order which contributes to the insulator-metal transition. At quarter-filling, a transition from the correlated insulating state to a semi-metallic state is observed as a function of tunneling ratio κ . This transition is characterized by charge gap, and C_2T symmetry. (Here, C_2T indicates 180-degree in-plane rotation symmetry C_2 with time reversal T .) The AFQMC results confirm that the ground states in both phases can be well described by a single determinant (i.e., solution of HF), in agreement with previous works using quantum chemistry methods (treating no valley degree of freedom) [38]. We also find a degenerate state with correlations between two valleys in the semi-metallic regime.

These results, in comparison with experimental observations, will also shed light on the modeling of MATBG. Although much needs to be done in this model, including fractional fillings, the systematic and accurate results at integer filling provide an important step in determining what additional ingredients, if any, will need to be considered to quantitatively describe MATBG.

The rest of the paper is organized as follows. In Sec. VII B, we briefly introduce the IBM model. In Sec. III, we introduce our AFQMC algorithm for studying Coulomb interaction with the topological band and its typical application in the IBM model. In Sec. IV, we describe the zero-temperature phase diagram of the IBM model at integer fillings. Finally, in Sec. V, we discuss connections with experiments comment on possible future work.

II. IBM MODEL

Our model consists of the continuum BM model \hat{H}_{BM} , which describes the moire bands at charge neutrality, and long-range screened Coulomb interactions \hat{V} . We briefly introduce IBM model here while elaborating more details in App. VII.

The continuum BM model \hat{H}_{BM} is a tight-binding model that describes electrons hopping between $2p_z$ orbitals of carbon atoms in twisted bilayer graphene. By taking Bloch vector \mathbf{p} , sub-lattice σ , and layer μ , spin s to identify the Bloch state (see Eq. 11), the continuum BM model can be written as:

$$\begin{aligned} \hat{H}_{BM} &= \sum_{\mathbf{p}} T_{\mathbf{p},\mathbf{p}}^{\text{intra}} c_{\mathbf{p}}^{\dagger} c_{\mathbf{p}} + T_{\mathbf{p}',\mathbf{p}}^{\text{inter}} c_{\mathbf{p}'}^{\dagger} c_{\mathbf{p}} \\ T_{\mathbf{p},\mathbf{p}}^{\text{intra}} &= \hbar\nu_F(p_x\sigma_x\tau_z + p_y\sigma_y) \\ T_{\mathbf{p}',\mathbf{p}}^{\text{inter}} &= \frac{1}{2} \sum_{l=0,1,2} \delta_{\mathbf{p}',\mathbf{p}-\tau_z\mathbf{q}_l} (\mu_x - i\mu_y) T_l + \text{h.c.} \\ T_l &= \omega_0 e^{-i\theta\sigma_z\mu_z\tau_z/2} + \omega_1 e^{2\pi i l\sigma_z\tau_z/3} \sigma_x e^{-2\pi i l\sigma_z\tau_z/3} \end{aligned} \quad (1)$$

where $\theta = 1.05^\circ$ is the twist angle, $\nu_F = 2700 * \frac{3a_0}{2\hbar}$ meV is the Dirac velocity, and ω_0, ω_1 describes lattice relaxation between A-A and A-B stacks, respectively. Transition momentum $\mathbf{q}_l = R(2\pi l/3)\mathbf{q}_0$, where $R(\psi) = e^{i\psi\sigma_y}$ is a rotation matrix. $\mathbf{q}_0 = \frac{8\pi\sin(\theta/2)}{3\sqrt{3}a_0}(0, -1)^T$ and $a_0 = 1.42\text{\AA}$ is the intra-layer distance between carbon atoms.

As two graphene layers stack with a twisted angle θ , the Brillouin zones (BZ) of mono-layer graphene rotate with angle θ related to the other layer, and this rotation leads to periodic moire pattern and folds BZ to mini-BZ (MBZ) [3]. That is we use $\varepsilon_{\mathbf{k},i}$ and $|\varphi_{\mathbf{k},i}\rangle$ to specify each band $n = 0, \dots, N_G - 1$ in MBZ:

$$\hat{H}_{BM}|\varphi_{\mathbf{k},i}\rangle = \varepsilon_{\mathbf{k},i}|\varphi_{\mathbf{k},i}\rangle \quad (2)$$

with $i = (n, \tau, s)$ to label bands n , valley τ , and spin s . N_G is truncated for numerical implementation.

We mention here that a correction term is included in addition to the BM model Hamiltonian \hat{H}_{BM} . The additional correction term, $[\hat{V}]_{\phi_{BM}}$, is a mean-field approximation of the Coulomb interactions \hat{V} with respect to the ground state ϕ_{BM} of the BM model at charge neutrality. This correction is adopted to remove or counter the double counting of the interaction effect [13, 28, 30], as parameters used in the BM model are based on first-principle calculations [3] which already account for the effect of Coulomb interactions at the density-functional theory level. There are somewhat different ways to treat the correction [31–33, 38], and the results turn out to be quite sensitive to the details of the correction. As we illustrate in Fig. 1, the band-structure of the dispersion part of the Hamiltonian, $\hat{H}_0 \equiv \hat{H}_{BM} - [\hat{V}]_{\phi_{BM}}$, can be significant different from that of \hat{H}_{BM} .

It is also important to mention that the model is parameterized by the ratio $\kappa = \omega_0/\omega_1$, which describes the lattice relaxation between AA regions (characterized by

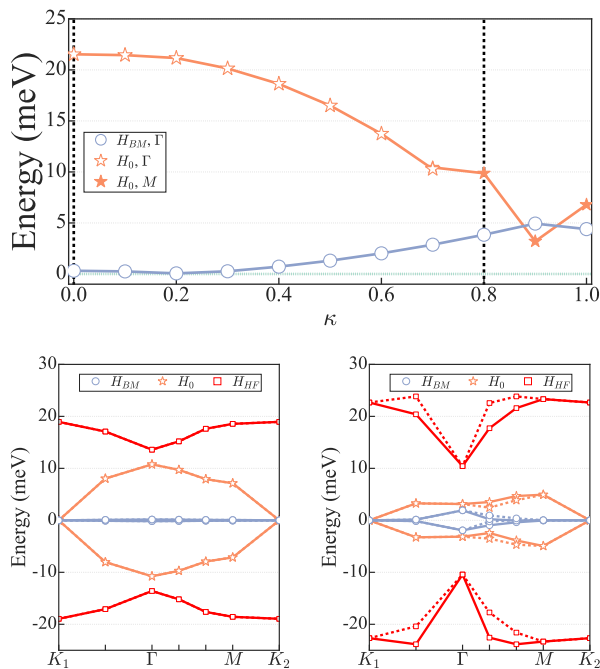


FIG. 1. (Top) Comparison of bandwidths between \hat{H}_{BM} and \hat{H}_0 versus κ in a 6×6 system. Γ and M label the \mathbf{k} -point where the largest gap is observed. (Bottom) Band structures of \hat{H}_0 , \hat{H}_{BM} and \hat{H}_{HF} for $\kappa = 0.0$ and $\kappa = 0.8$. \hat{H}_{HF} indicates the IBM model band structure obtained from Hartree-Fock (HF). Solid and dashed lines specify the two valleys respectively (degenerate at $\kappa = 0$).

ω_0) and AB&BA regions (characterized by ω_1). This ratio κ is responsible for the emergence of flat bands [10] and the ground state symmetry [13, 14]. To explore the effects of lattice relaxation in TBG, we fix $\omega_1 = 105\text{meV}$ and study $\kappa \in (0, 1)$, which covers the entire range from the chiral limit ($\kappa = 0$) through the more realistic case ($\kappa \sim 0.8$).

The IBM model is built based on eight “flat” bands (i.e., two bands with two valleys and two spins that are closest to the Fermi surface) from the BM model. Effect from the remote bands are neglected. The Hamiltonian of our IBM model is

$$\begin{aligned} \hat{H}_{IBM} &= \hat{H}_0(\kappa) + \hat{V} \\ &= \sum_{\mathbf{k}, i} \varepsilon_{\mathbf{k}, i} c_{\mathbf{k}, i}^\dagger c_{\mathbf{k}, i} - \sum_{\mathbf{k}, i, j} [V]_{\mathbf{k}, i; \mathbf{k}, j} c_{\mathbf{k}, i}^\dagger c_{\mathbf{k}, j} + \frac{1}{2} \sum_{\mathbf{q}} \bar{\rho}_{\mathbf{q}} V_{\mathbf{q}} \bar{\rho}_{-\mathbf{q}} \end{aligned} \quad (3)$$

where \mathbf{k} is on a hexagonal lattice with size L to discretize the first MBZ (see Fig. 9), $\bar{\rho}_{\mathbf{q}}$ is the density operator at momentum $\mathbf{q} = \mathbf{k} - \mathbf{k}'$ with a background shift [49], and $V_{\mathbf{q}}$ is the Fourier transformed Coulomb potential. The transfer momentum \mathbf{q} remains unrestricted, but is truncated for numerical implementation. The Coulomb

potential is two-gate screened:

$$V_{\mathbf{q}} = \frac{e^2}{2\epsilon\epsilon_0} \frac{1}{A} \frac{\tanh(|\mathbf{q}|d)}{|\mathbf{q}|}. \quad (4)$$

which is the Fourier-transformed Coulomb potential with the distance $d = 20$ nm between two layers and relative permittivity $\epsilon = 10$ for vacuum permittivity ϵ_0 . We comment on the choice of relative permittivity in App. XI. $A = N_M A_0$ is the total area of the system with $A_0 = \sqrt{2} a_M^2 / 2$, $a_M = \sqrt{3} a_0 / 2 \sin \frac{\theta}{2} = 13.4$ nm and N_M is the number of moire unite cells of this system.

III. AFQMC WITH PHASELESS CONSTRAINT

The IBM model is a much simplified model, which still contains both a non-trivial band-structure, including corrections, and long-range Coulomb interaction. The phaseless AFQMC [44] has the capacity to study such a general Hamiltonian while controlling the sign problem to restore low-polynomial computational scaling with lattice sizes. To give a brief self-contained description, we adopt the notation in Ref. [49] and start from the Hamiltonian we treat, written in “Monte Carlo form”:

$$\hat{H} = \hat{T} + \frac{1}{2} \sum_{\gamma} \hat{L}_{\gamma}^2 \quad (5)$$

where \hat{T} and \hat{L}_{γ} denote sets of one-body operators whose matrix elements are explicitly specified in the chosen basis. To study the IBM model, we take $\hat{L}_{\mathbf{q}} = \sqrt{\frac{V_{\mathbf{q}}}{2}} (\bar{\rho}_{\mathbf{q}} + \bar{\rho}_{-\mathbf{q}})$ and $\hat{L}'_{\mathbf{q}} = i\sqrt{\frac{V_{\mathbf{q}}}{2}} (\bar{\rho}_{\mathbf{q}} - \bar{\rho}_{-\mathbf{q}})$ [47].

AFQMC performs ground-state calculations through the imaginary-time projection:

$$\begin{aligned} |\Psi_0\rangle &\propto \lim_{\beta \rightarrow \infty} e^{-\beta \hat{H}} |\phi_I\rangle \\ &\approx (e^{-\tau \hat{H}})^n |\phi_I\rangle \\ &\approx \int d\{\mathbf{x}\} \prod_{i=1}^n p(\mathbf{x}_i) \hat{B}(\mathbf{x}_i) |\phi_I\rangle, \end{aligned} \quad (6)$$

which propagates the given initial state $|\phi_I\rangle$ to the ground state $|\Psi_0\rangle$ of the Hamiltonian \hat{H} , if the overlap $\langle \Psi_0 | \phi_I \rangle$ is non-zero. The second line of Eq. (6) is obtained by using the Suzuki-Trotter decomposition [52, 53] to break the imaginary-time evolution operator into time slices with $n = \beta/\tau$. The third line is then obtained by applying the Hubbard-Stratonovich transformation [54, 55] to decouple the short-time propagator in each time slice with probability

$$p(\mathbf{x}) = \prod_{\gamma} \frac{1}{\sqrt{2\pi}} e^{-x_{\gamma}^2/2}, \quad (7)$$

and the one-body propagator

$$\hat{B}(\mathbf{x}) = e^{-\tau \hat{T}/2} e^{\sum_{\gamma} x_{\gamma} \sqrt{-\tau} \hat{L}_{\gamma}} e^{-\tau \hat{T}/2}, \quad (8)$$

where \mathbf{x} indicates a series of auxiliary-fields (AFs): $\mathbf{x} = \{x_\gamma\}$ ($x_\gamma \in \mathbb{R}$). Without loss of generality, we can take $|\phi_I\rangle$ as a single determinant. Since a one-body propagator propagates a single determinant to another single determinant: $|\phi'\rangle = \hat{B}(\mathbf{x})|\phi\rangle$, the integration in Eq. (6) can then be performed by Monte Carlo, mapping the sampling of $\{x_\gamma\}$ into random walks in the manifold of Slater determinants along the direction of imaginary time evolution [46].

Because of fermion antisymmetry, the Monte Carlo sampling of Eq. (6) in general suffers from a phase problem [44]. The phase problem in AFQMC can be understood by considering [46] a single determinant, through random chance in the time evolution, becoming perpendicular to the ground state, after which propagation of this determinant effectively contributes nothing but statistical fluctuations to the ground state estimation. Since the number of such determinants in general grows exponentially with projection time, the signal of Monte Carlo sampling will eventually be overwhelmed by statistic noise. Eliminating these determinants that are perpendicular to the ground state is an exact condition which removes the sign or phase problem [44, 45]. To implement this condition, AFQMC uses a trial wave function $|\Psi_T\rangle$ to constrain the random walk paths. For the general form of interaction, the orbitals in the Slater determinant become complex, effectively introducing an overall gauge degree of freedom that is redundant in the projection. The constraint in this case is a phaseless approximation that projects the weight of each Slater determinant sample to the real axis in the complex plane [49]. If the trial wave function is the exact ground state, then this constraint is unbiased. Many community benchmark studies have shown that AFQMC with constraint is highly accurate, both in model systems and in real materials [56–58].

To further validate the accuracy and robustness of the phaseless AFQMC approach in this study, we have taken several additional measures. In the IBM model different low-lying states of different symmetry characters can be (nearly) degenerate. The AFQMC method we use is in general much less prone to ergodicity problems in the sampling, because it takes the form of many (almost independent) streams of branching random walks. Still, we perform multiple AFQMC calculations using different low-lying HF states of different symmetry as trial/initial wave function. The final energy is compared to gauge the preferred symmetry of the many-body ground state. (Although the ground-state energy computed by AFQMC is not strictly variational [59], the energy is very accurate, and we only draw conclusions about the ordering of the states when the energy separation is much more significant than the expected resolution of the phaseless approximation.) For the study of $n_f = 2, 4$, C_2T -symmetry-breaking states and K-IVC states are barely distinguishable in energy around the chiral limit. In these cases, we apply yet another step, using a constraint release method, AFQMC with Metropolis release constraint (AFQMC-MRC) [60], to minimize the constraint

bias and identify the actual symmetry of the ground state. Further details are given in the App. IX.

To summarize, in this work, we employ AFQMC to systematically investigate the IBM model. Compared with previous quantum Monte Carlo work [30, 31, 33], this method is not limited to special fillings, high temperatures, or small system sizes. It allows us to access the whole range of κ to determine the complete phase diagram (with the largest lattice up to 12×12), while treating both valley and spin degrees of freedom.

IV. RESULTS

In this section, we describe our numerical results for the ground state of the IBM model from AFQMC, divided into several subsections by filling fractions: charge neutrality ($n_f = 4$) and half-filling ($n_f = 2$), quarter-filling ($n_f = 1$), and three-quarter-filling ($n_f = 3$). The tunneling ratio κ for realistic cases varies sample by sample and can affect the ground state behaviors. To present a systematic study and facilitate comparison with experiments, this work scans κ from 0 to 1. At the flat band limit, analytical studies [13, 14] indicate that the candidate ground states are correlated insulating states: quantum anomalous Hall (QAH) state, valley Hall (VH) state and K-IVC state for fillings $n_f = 4$ and 2, and QAH for filling $n_f = 1$. HF results (on the IBM model but with no double counting correction) [26] support the above analysis and suggest the ground state at $n_f = 3$ filling is a mixture of the states at $n_f = 4, 2$ and $n_f = 1$ fillings. As discussed in the last paragraph of Sec. III, we can use each of the candidate symmetry states above as the trial wave function in AFQMC. In this sense, our calculations can be viewed as using an unbiased (or at least less biased than other possibilities) method, namely AFQMC, to judge the validity of the different candidates as the many-body ground state.

Our results show that the HF solution is in some cases quite accurate, while in other situations qualitatively incorrect. It is worth emphasizing that, while a weakly interacting system is often well described by a single determinant solution from a mean-field calculation, the reverse is not always true. That is, a system which can be described well by a single Slater determinant is not necessarily weakly interacting. An example of this is the Wigner crystal state in the electron gas at the low-density limit, an essentially classical state whose energy can be well approximated by that of a single-determinant solution in the spirit of unrestricted HF, but which is a strongly interacting state, with the interaction energy dominating the kinetic (zero-point) energy. In the IBM, the system is often more analogous to this situation when the HF solution is accurate. We quantify the errors from mean-field theory calculations throughout the parameter regimes.

A. Breaking of K-IVC insulating state at $n_f = 4$ and $n_f = 2$

At $n_f = 4$ and $n_f = 2$ fillings, we observe a transition from a metallic state to a K-IVC insulating state. At large κ ($\kappa > \sim 0.8$), we find the ground states are K-IVC states characterized by a spontaneous hybridization between the two valleys that preserves an effective time-reversal symmetry. The K-IVC state occupies both spins at charge neutrality and is polarized at one spin at half-filling. This is also the picture from the HF solution, but quantitative discrepancies are seen between HF and AFQMC. In contrast, at small κ (i.e., $\kappa < \sim 0.2$) we observe qualitative differences from the HF solution. The system is characterized by much larger correlation energy, a loss of long range K-IVC order, and vanishing charge gap. Below we first show our observation of this insulator-metal transition through the ground-state energy, including correlation energy, followed by results on the charge gap. Then we study the K-IVC order parameter and band occupancy to complete this discussion.

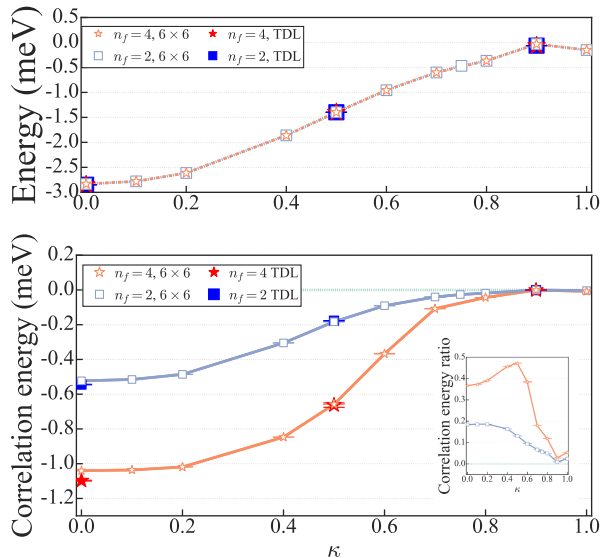


FIG. 2. Ground-state energies and correlation energies. The top panel shows the HF energy per electron, E_{HF} , as a function of κ , for both $n_f = 4$ and $n_f = 2$. The bottom panel shows the corresponding correlation energies, E_c . Most results are obtained from a 6×6 lattice in momentum space, but at three values of κ results are also shown for the thermodynamic limit (TDL), which is obtained via extrapolation with 6×6 , 9×9 , and 12×12 lattices. The inset in the bottom panel shows the correlation energy relative to the total, $|E_c|/E_{\text{HF}}$.

In Fig. 2, we show the HF energy per electron, E_{HF} , and the AFQMC correction over HF (i.e., the correlation energy) versus κ . The correlation energy is an important metric widely adopted in electronic structure calculations and quantum chemistry, defined as the difference between the true many-body ground-state energy and that from

HF, which in this case is $E_c \equiv E_{\text{AFQMC}} - E_{\text{HF}}$, where E_{AFQMC} is the ground-state energy per electron from AFQMC (calculated by the mixed estimator [44, 49], with the HF state as the trial wave function). For $n_f = 2$, HF yields a spin-polarized K-IVC state; for $n_f = 4$, it finds a superposition of two spin-polarized K-IVC states with opposite spins and no correlation between them. The K-IVC states at the two fillings have exactly the same HF energy per electrons, since the mean-field background of Coulomb interaction is removed in Eq. (3) by shifting the charge-density operators according to the chemical potential at the corresponding filling n_f . In the chiral limit ($\kappa = 0$), HF yields an emergent C_2T -symmetry-breaking (QAH, VH) state that preserves $U_V(1)$ symmetry at both fillings and is degenerate with the K-IVC state. Both the K-IVC and the C_2T -symmetry-breaking states are correlated insulating states. Details of the above analysis are elaborated in App. VIII. The above observation agrees with previous analytical studies [13, 14] and the numerical HF results [26]. To simplify our studies, we focus on the K-IVC state here, but briefly discuss the close competition between it and the C_2T -symmetry-breaking state in App. IX.

The amount of correlation energy $|E_c|$ grows as κ decreases, as seen in the bottom panel of Fig. 2. Beyond $\kappa = 0.9$ virtually no correlation energy is present, making the HF description essentially exact. At lower κ many-body correlations make significant corrections to the HF results, which could render perturbative analysis more problematic. Interestingly, although the correlation energy magnitude decreases monotonically with κ , the percentage of the correlation energy relative to the total ground-state energy (here measured with respect to the HF energy) is not monotonic, reaching a maximum at intermediate κ for $n_f = 4$, as seen in the inset of the bottom panel. We also observe a strong manifestation of correlation effects in the separation of the $n_f = 4$ and $n_f = 2$ curves, in contrast with previous analytical predictions [13, 14] around the “flat” band limit. Correlation between different spins leads to a dramatic lowering of the $n_f = 4$ correlation energy from the spin-polarized state.

We next examine the ground state properties in some detail. We compute the charge gap of the system via the add/remove energy:

$$\Delta_c = \frac{E(N+1) + E(N-1) - 2E(N)}{2}, \quad (9)$$

where N is the total number of electrons in the simulation cell at the targeted filling fraction, and $E(N)$ is the total ground-state energy. The results are shown in Fig. 3 as a function of κ for both $n_f = 4$ and $n_f = 2$. At $\kappa \approx 0.9$, AFQMC finds the same finite charge gaps as HF at both fillings, which is consistent with the picture from Fig. 2 and confirms the K-IVC ground states in this regime. As κ decreases, we observe a quantitative difference between the two filling fractions, with the charge gap increasing for $n_f = 4$ and remaining essen-

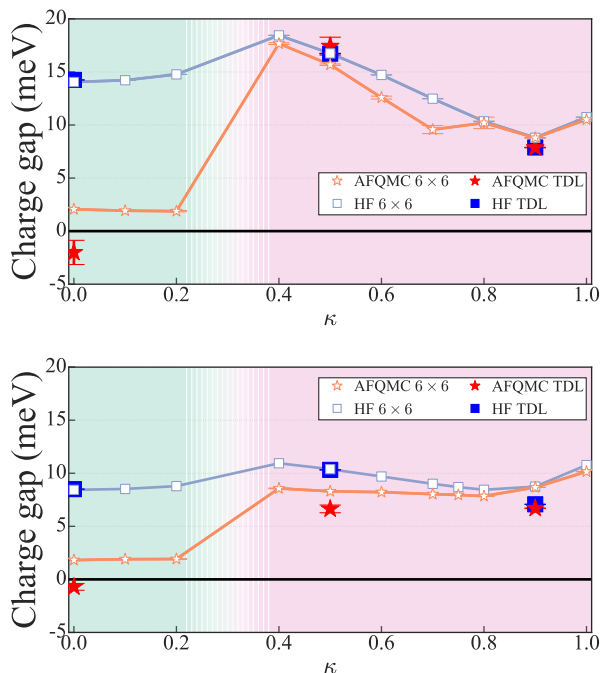


FIG. 3. Charge gaps versus κ at $n_f = 4$ (top panel) and $n_f = 2$ (bottom panel). Similar to Fig. 2, a 6×6 lattice is used in the calculations, but spot checks are performed at $\kappa = 0.0, 0.5$, and 0.9 by extrapolating through 6×6 , 9×9 , and 12×12 lattices for the TDL. Shaded pink and green backgrounds separating the semi-metallic and insulating phases are a rough guide to the eye.

tially constant for $n_f = 2$, until κ reaches an intermediate value around 0.4 , when a sharp drop in Δ_c is seen at both fillings. As κ further decreases, the AFQMC charge gap is much reduced compared to the HF gap. A more careful finite-size scaling study, as illustrated for $\kappa = 0$, shows that Δ_c from AFQMC becomes vanishingly small at the TDL, while the gap from HF remains very large. Thus, contrary to the HF prediction, the many-body state is metallic at small κ at both fillings, with a metal-insulator transition taking place roughly around $\kappa \sim 0.3$.

To better characterize the ground-state phases, we also compute the K-IVC order parameter and band occupancy. Expectation values of operators that commute with the Hamiltonian, such as the ground-state energies and gaps discussed above, can be computed by the so-called mixed estimator [44] in AFQMC. Other expectations require additional technical steps to compute, for example by back-propagation [45, 61] or via linear response [62, 63]. We take the latter approach here, which requires separate calculations for different expectations but tends to be more accurate. More specifically, we calculate the expectation value of an operator \hat{O} with respect to the ground state from AFQMC, $\langle \hat{O} \rangle$,

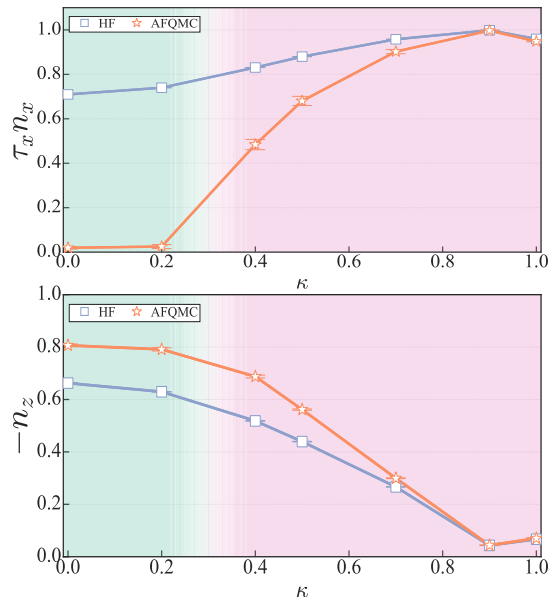


FIG. 4. K-IVC order parameter (top) and band occupancy (bottom) versus κ at $n_f = 2$ filling. Results are obtained with a 6×6 lattice. Shaded pink and green backgrounds separate the metallic/semi-metallic and insulating phases as in Fig. 3.

via Hellman-Feynman theorem

$$\langle \hat{O} \rangle = \lim_{\lambda \rightarrow 0} \frac{d \langle \hat{H}_{IBM} + \lambda \hat{O} \rangle}{d\lambda}, \quad (10)$$

which is then evaluated by finite difference with several ground-state energy calculations at small λ . Further details are given in App. X.

In Fig. 4, we show the computed K-IVC order parameter $\langle \tau_x n_x \rangle$ and band occupancy $\langle -n_z \rangle$ for different κ at $n_f = 2$ filling. The subscripts of n_* and τ_* denote the related Pauli operator on bands and valleys (i.e., $\tau_x n_x = \frac{1}{L^2} \sum_{\mathbf{k}, s} c_{\mathbf{k}, i' = (-n, -\tau, s)}^\dagger c_{\mathbf{k}, i = (n, \tau, s)}$, and $n_z = -n \frac{1}{L^2} c_{\mathbf{k}, i}^\dagger c_{\mathbf{k}, i}$ with $\tau = 1$ for + valley and $\tau = -1$ for - valley, $n = 1$ for top band and $n = -1$ for bottom band.) The K-IVC order parameter is used to identify the strength of K-IVC order (see App. VIII) and the band occupancy shows the difference in electron distributions between the top and bottom bands. At $\kappa = 0.9$, a strong signal of K-IVC order is seen, and electrons are almost evenly distributed over the top and bottom bands. These observations again confirm a K-IVC ground state. As κ decreases, we find a decay of the K-IVC order in both the HF and AFQMC results. However, the K-IVC order in AFQMC decays much faster, and vanishes at $\kappa \sim 0.2$, while in HF it stays at a significant finite value. In the bottom panel the band occupancy increases as κ decreases. A large $\langle -n_z \rangle$ implies a higher occupancy of the bottom bands. The computed value from AFQMC is always larger than from HF, indicating that the electrons tend to stay in the bottom bands more. Since electrons forming K-IVC pairs tend to be evenly distributed over

the top/bottom band, the results on $\langle -n_z \rangle$ suggest a decay of K-IVC order with decreasing κ , consistent with $\langle \tau_x n_x \rangle$. By symmetry [13], the above analysis and observations can be directly applied to $n_f = 4$ filling.

We also examined the stability of a fully spin-polarized ground state for $n_f = 2$ and non-spin-polarized ground state for $n_f = 4$ by computing the energy cost for flipping spins. These results are included in App. IX.

B. Breaking of C_2T symmetry at $n_f = 1$

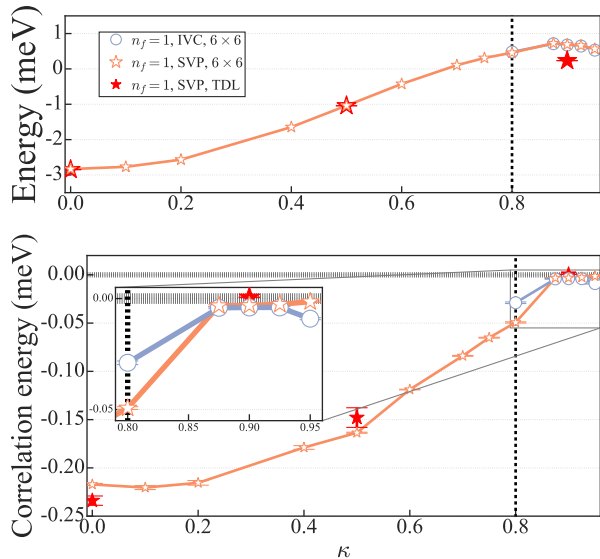


FIG. 5. Ground-state energies and correlation energies for spin valley polarized (SVP) state and inter-valley coherent (IVC) state, at $n_f = 1$. The top panel shows the HF energy per electron, E_{HF} , as a function of κ , for the two types of states considered. The bottom panel shows the corresponding correlation energies, E_c . Most results are obtained from a 6×6 lattice in momentum space, but at three values of κ results are shown for the SVP state at the TDL, using the same extrapolation procedure as in Fig. 2. Beyond $\kappa = 0.8$ (indicated by the vertical black dashed lines) the SVP and IVC states are degenerate within HF, while small energy differences are seen in AFQMC. However when extrapolated to the TDL at $\kappa = 0.85$, the energy difference in AFQMC is zero within statistical error bar.

At $n_f = 1$, we find that the ground state can be reasonably approximated by HF through a comparison between HF and AFQMC results in both correlation energy and charge gap. This is consistent with results from a previous quantum chemistry study [38]. Based on HF, we observed a transition along κ from the C_2T -symmetry-breaking correlated insulating state (i.e., Chern polarized QAH state [13]) to a C_2T -symmetry-restored semi-metallic state and an emerged spin-polarized inter-valley-correlated semi-metallic state.

In Fig. 5, we show HF energy in the top panel and the AFQMC correction over HF in the bottom panel for

different κ at $n_f = 1$. Our HF study found a spin-valley-polarized (SVP) state for all κ , and a spin-polarized inter-valley coherent (IVC) state at $\kappa \geq 0.8$. In the bottom panel, the same correlation energy behaviors are seen as observed for $n_f = 4, 2$, where many-body effects are found to be strong at the chiral limit (i.e., $\kappa = 0$) and become vanishingly small at large κ . However, the correlation energy for $n_f = 1$ is much smaller than in $n_f = 4, 2$, and AFQMC only leads to a quantitative correction over HF.

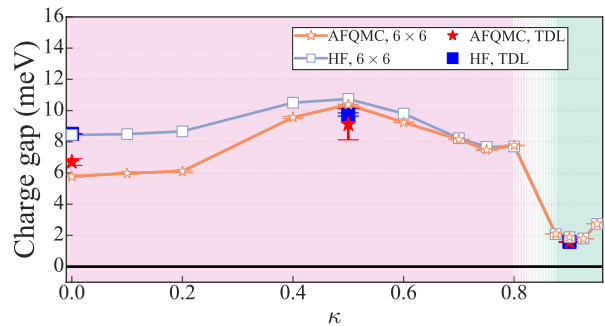


FIG. 6. Charge gap for $n_f = 1$ filling versus κ . Charge gaps are calculated by measuring the energy required to add or remove an electron from the system. AFQMC proceeds with the corresponding HF state as the trial wave function, whose HF charge gap is illustrated in the figure. The thermodynamic limits (TDL) are extrapolated through 6×6 , 9×9 , and 12×12 lattice calculations. Shaded pink and green backgrounds separate the metallic/semi-metallic and insulating phases.

In Fig. 6, we show the charge gap for different κ . A finite charge gap is seen for $\kappa < 0.8$ at the thermodynamic limit, which suggests an insulating ground state. A sudden drop of the charge gap is observed around $\kappa = 0.8$, indicating a transition to semi-metallic states. This behavior, however, is quite different from what is observed at $n_f = 4, 2$, where mean-field calculations do not capture the metallic states that emerge.

In Fig. 7, we show that the above insulating-semi-metallic transition is accompanied by a restoration of C_2T -symmetry and an emerge of IVC state. Since our energy and charge gap results show only minor differences between AFQMC and HF here, we consider the HF state as a qualitatively good approximation for the ground state, and we use HF to study the behavior of IVC and C_2T -symmetry by focusing on the K-IVC order parameter $\langle \tau_x n_x \rangle$ and the C_2T -symmetry-breaking order parameter $C(gK)$ proposed in [38], following identical notation (g is unitary symmetry and K is complex conjugation). $C(gK)$ vanishes when C_2T symmetry is completely restored. At small κ , the ground state is well described by a spin-valley polarized QAH state where C_2T -symmetry is significantly broken, and no K-IVC order is observed. As κ increases, a degeneracy of the SVP state and spin-polarized IVC state is seen. For the SVP state, a sudden drop of $C(gK)$ indicates a restoration

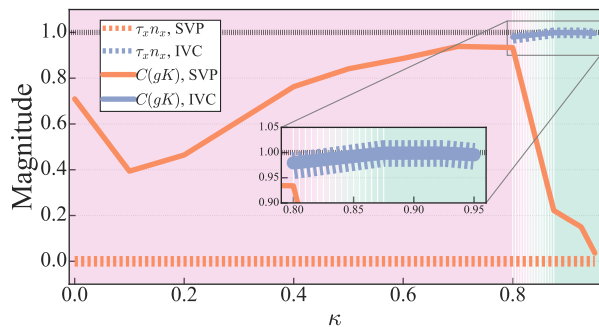


FIG. 7. K-IVC order parameter $\tau_x n_x$ and C_2T -symmetry-breaking order parameters $C(gK)$ at $n_f = 1$ for HF ground states with spin-valley-polarized (SVP) or Inter-valley coherent (IVC) symmetry breaking. In the degenerate region (i.e., between $\kappa = 0.8$ and $\kappa = 0.95$), HF states are determined by imposing the spin-polarized/inter-valley-coherent initial density, respectively. Shaded green and pink backgrounds separate the insulating and metallic/semi-metallic phases as in Fig. 6.

of C_2T -symmetry. For the spin-polarized IVC state, we find a significant K-IVC order parameter with significant C_2T symmetry breaking. Remarkably, $\tau_x n_x \sim 1$ suggests all electrons at $n_f = 1$ form K-IVC pairs, but this is not a K-IVC state found in $n_f = 4, 2$ as there are not enough K-IVC pairs to fill entire valence bands.

C. Mixture at $n_f = 3$

At $n_f = 3$ filling, we observed a “phase diagram” as a function of κ that shows features from both $n_f = 2$ and $n_f = 1$. In Fig. 8, we show the charge gap for different κ . For the HF study, we observed a K-IVC state polarized at one spin flavor and a C_2T -symmetry-breaking state polarized at the other spin and one valley, which agrees with previous results [26]. For the AFQMC study, we also observed a combination of two states in the many-body sense. We observed a metallic state for small κ , and a transition to an insulating state as κ is increased. As $\kappa \sim 0.8$ is approached, the drop in the charge gap is observed, which suggests a semi-metallic state. This behavior can be understood as a result of the direct combination between the state at $n_f = 2$ and $n_f = 1$.

V. SUMMARY AND DISCUSSION

In this work, we investigated a model for twisted bilayer graphene that combines the BM model with realistic electron-electron Coulomb interactions. To minimize the difference between real materials and the model, we consider a mean-field correction to remove the double counting of Coulomb interactions and tune the ratio κ to include the effects of lattice relaxation. We employ HF

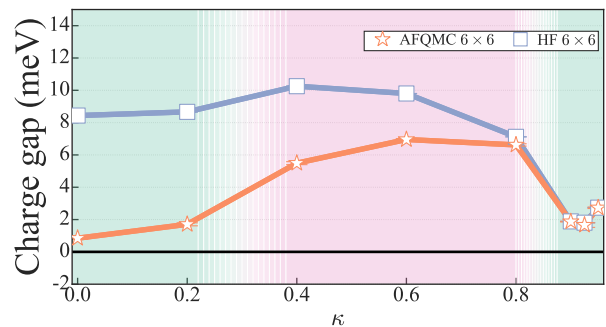


FIG. 8. Charge gap for $n_f = 3$ filling versus κ . AFQMC calculations use the corresponding HF state as the trial wave function, whose charge gap is also shown in the figure. Shaded pink and green backgrounds separate the metallic/semi-metallic and insulating phases.

and AFQMC to study this model at three typical integer fillings, in order to probe and quantify the effect of electron correlation.

We implemented state-of-the-art phaseless AFQMC to enable an accurate and systematic study of the ground state of the IBM model for a range of parameters and fillings. By controlling the sign problem with the phaseless constraint, we perform calculations in the ground state and in lattices as large as 12×12 to reach the thermodynamic limit. Numerical Hartree Fork is first carried out to produce mean-field candidates of the ground states. Based on symmetry breaking in perturbation theories, these mean-filled states are correlated insulating states with either K-IVC or C_2T symmetry breaking. We then use the HF states as trial wave functions for AFQMC and determine the actual ground states. The work presented here paves the way for systematic studies of realistic models of MATBG. The same AFQMC technology we have set up can be directly applied to reach beyond the integer fillings studied here. It can also be adopted to study the effect of Kekulé phonons via a non-retarded two-body attraction [64, 65].

The outcome of these calculations is summarized as ground state phase diagrams for the IBM model for different integer fillings as a function of the tunneling ratio κ . Our results at charge neutrality are consistent with those from previous sign-problem-free QMC studies which focused on limited parameters [30, 31, 33]. At charge neutrality and half-filling, we observe an insulator-metal transition with a loss of spin gap and K-IVC long-range order. The results suggest that this transition is the result of many-body effects driven by competition between topological band and Coulomb interaction. At quarter-filling, we observe an insulator-metal transition that comes with a restoration of C_2T symmetry and an emerged inter-valley-correlated state. Our results indicate that the transition can be qualitatively described by HF. We observe the restoration of C_2T symmetry confirming conclusions of a previous study which did not

include valley degree of freedom [38]. An extra spin-polarized IVC state is seen in our study. We also investigate the ground state phase diagram at three-quarter-filling. As a function of κ it shows both features from both charge neutrality/half-filling and quarter-filling.

We find that the ground state of the IBM model is very sensitive to the corrections of the bare band structure. This has also been seen in other many-body studies [30, 36, 38]. Though conclusions from many-body studies, including ours, appear to yield qualitatively consistent results, the detailed model in each work involves different mean-field corrections, which lead to quantitative discrepancies. We believe it would be very valuable to have a single model to study. Agreement between different many-body calculations would then help “converge” a set of reliable solutions to the model. Discrepancies between different methods would help identify areas of improvement needed and spur method development and synergistic studies [57, 58].

For example, recent experiments [19] suggest the ground state of twisted bilayer graphene is in a time-reversal symmetric inter-valley coherent (T-IVC) phase, while a small strain can lead to incommensurate Kekulé

spiral (IKS) order. Are these states captured by the IBM model but not by the detailed Hamiltonian we (and others) have studied? Or are there limitations in our computations? The aforementioned unique model and converged solution would allow more direct comparisons with experimental observations, which can then identify model limitations, and improve our understanding of essential physics.

VI. ACKNOWLEDGMENTS

We thank L. Lin, A. H. MacDonald, O. Vafek for helpful conversations. Z.X. acknowledges partial support from the U.S. Department of Energy (DOE) under grant DE-SC0001303. Z.X. is also grateful for the support and hospitality of the Center for Computational Quantum Physics (CCQ), where this work was performed. Computing was carried out at the computational facilities at Flatiron Institute. The Flatiron Institute is a division of the Simons Foundation.

-
- [1] Y. Cao, V. Fatemi, A. Demir, S. Fang, S. L. Tomarken, J. Y. Luo, J. D. Sanchez-Yamagishi, K. Watanabe, T. Taniguchi, E. Kaxiras, R. C. Ashoori, and P. Jarillo-Herrero, Correlated insulator behaviour at half-filling in magic-angle graphene superlattices, *Nature* **556**, 80 (2018).
- [2] Y. Cao, V. Fatemi, S. Fang, K. Watanabe, T. Taniguchi, E. Kaxiras, and P. Jarillo-Herrero, Unconventional superconductivity in magic-angle graphene superlattices, *Nature* **556**, 43 (2018).
- [3] R. Bistritzer and A. H. MacDonald, Moiré bands in twisted double-layer graphene, *Proceedings of the National Academy of Sciences* **108**, 12233 (2011), <https://www.pnas.org/doi/pdf/10.1073/pnas.1108174108>.
- [4] C. Xu and L. Balents, Topological superconductivity in twisted multilayer graphene, *Phys. Rev. Lett.* **121**, 087001 (2018).
- [5] J. Kang and O. Vafek, Symmetry, maximally localized wannier states, and a low-energy model for twisted bilayer graphene narrow bands, *Phys. Rev. X* **8**, 031088 (2018).
- [6] M. Xie and A. H. MacDonald, Nature of the correlated insulator states in twisted bilayer graphene, *Phys. Rev. Lett.* **124**, 097601 (2020).
- [7] J. F. Dodaro, S. A. Kivelson, Y. Schattner, X. Q. Sun, and C. Wang, Phases of a phenomenological model of twisted bilayer graphene, *Phys. Rev. B* **98**, 075154 (2018).
- [8] L. Zou, H. C. Po, A. Vishwanath, and T. Senthil, Band structure of twisted bilayer graphene: Emergent symmetries, commensurate approximants, and wannier obstructions, *Phys. Rev. B* **98**, 085435 (2018).
- [9] Z. Bi, N. F. Q. Yuan, and L. Fu, Designing flat bands by strain, *Phys. Rev. B* **100**, 035448 (2019).
- [10] G. Tarnopolsky, A. J. Kruchkov, and A. Vishwanath, Origin of magic angles in twisted bilayer graphene, *Phys. Rev. Lett.* **122**, 106405 (2019).
- [11] J. Kang and O. Vafek, Strong coupling phases of partially filled twisted bilayer graphene narrow bands, *Phys. Rev. Lett.* **122**, 246401 (2019).
- [12] K. Seo, V. N. Kotov, and B. Uchoa, Ferromagnetic mott state in twisted graphene bilayers at the magic angle, *Phys. Rev. Lett.* **122**, 246402 (2019).
- [13] N. Bultinck, E. Khalaf, S. Liu, S. Chatterjee, A. Vishwanath, and M. P. Zaletel, Ground state and hidden symmetry of magic-angle graphene at even integer filling, *Phys. Rev. X* **10**, 031034 (2020).
- [14] E. Khalaf, S. Chatterjee, N. Bultinck, M. P. Zaletel, and A. Vishwanath, Charged skyrmions and topological origin of superconductivity in magic-angle graphene, *Science Advances* **7**, eabf5299 (2021), <https://www.science.org/doi/pdf/10.1126/sciadv.abf5299>.
- [15] B. Lian, Z.-D. Song, N. Regnault, D. K. Efetov, A. Yazdani, and B. A. Bernevig, Twisted bilayer graphene. iv. exact insulator ground states and phase diagram, *Phys. Rev. B* **103**, 205414 (2021).
- [16] Y. H. Kwan, G. Wagner, T. Soejima, M. P. Zaletel, S. H. Simon, S. A. Parameswaran, and N. Bultinck, Kekulé spiral order at all nonzero integer fillings in twisted bilayer graphene, *Phys. Rev. X* **11**, 041063 (2021).
- [17] M. I. B. Utama, R. J. Koch, K. Lee, N. Leconte, H. Li, S. Zhao, L. Jiang, J. Zhu, K. Watanabe, T. Taniguchi, P. D. Ashby, A. Weber-Bargioni, A. Zettl, C. Jozwiak, J. Jung, E. Rotenberg, A. Bostwick, and F. Wang, Visualization of the flat electronic band in twisted bilayer graphene near the magic angle twist, *Nature Physics* **17**, 184 (2021).

- [18] S. Lisi, X. Lu, T. Benschop, T. A. de Jong, P. Stepanov, J. R. Duran, F. Margot, I. Cucchi, E. Cappelli, A. Hunter, A. Tamai, V. Kandyba, A. Giampietri, A. Barinov, J. Jobst, V. Stalman, M. Leeuwenhoek, K. Watanabe, T. Taniguchi, L. Rademaker, S. J. van der Molen, M. P. Allan, D. K. Efetov, and F. Baumberger, Observation of flat bands in twisted bilayer graphene, *Nature Physics* **17**, 189 (2021).
- [19] K. P. Nuckolls, R. L. Lee, M. Oh, D. Wong, T. Soejima, J. P. Hong, D. Călugăru, J. Herzog-Arbeitman, B. A. Bernevig, K. Watanabe, T. Taniguchi, N. Regnault, M. P. Zaletel, and A. Yazdani, Quantum textures of the many-body wavefunctions in magic-angle graphene (2023), arXiv:2303.00024 [cond-mat.mes-hall].
- [20] J. Ahn, S. Park, and B.-J. Yang, Failure of nielsen-ninomiya theorem and fragile topology in two-dimensional systems with space-time inversion symmetry: Application to twisted bilayer graphene at magic angle, *Phys. Rev. X* **9**, 021013 (2019).
- [21] H. C. Po, L. Zou, T. Senthil, and A. Vishwanath, Faithful tight-binding models and fragile topology of magic-angle bilayer graphene, *Phys. Rev. B* **99**, 195455 (2019).
- [22] Z.-D. Song, B. Lian, N. Regnault, and B. A. Bernevig, Twisted bilayer graphene. ii. stable symmetry anomaly, *Phys. Rev. B* **103**, 205412 (2021).
- [23] M. Koshino, N. F. Q. Yuan, T. Koretsune, M. Ochi, K. Kuroki, and L. Fu, Maximally localized wannier orbitals and the extended hubbard model for twisted bilayer graphene, *Phys. Rev. X* **8**, 031087 (2018).
- [24] Z.-D. Song and B. A. Bernevig, Magic-angle twisted bilayer graphene as a topological heavy fermion problem, *Phys. Rev. Lett.* **129**, 047601 (2022).
- [25] G. Rai, L. Crippa, D. Călugăru, H. Hu, L. de' Medici, A. Georges, B. A. Bernevig, R. Valentí, G. Sangiovanni, and T. Wehling, Dynamical correlations and order in magic-angle twisted bilayer graphene (2023), arXiv:2309.08529 [cond-mat.str-el].
- [26] Y. Zhang, K. Jiang, Z. Wang, and F. Zhang, Correlated insulating phases of twisted bilayer graphene at commensurate filling fractions: A hartree-fock study, *Phys. Rev. B* **102**, 035136 (2020).
- [27] S. Zhang, X. Lu, and J. Liu, Correlated insulators, density wave states, and their nonlinear optical response in magic-angle twisted bilayer graphene, *Phys. Rev. Lett.* **128**, 247402 (2022).
- [28] S. Liu, E. Khalaf, J. Y. Lee, and A. Vishwanath, Nematic topological semimetal and insulator in magic-angle bilayer graphene at charge neutrality, *Phys. Rev. Res.* **3**, 013033 (2021).
- [29] P. Potasz, M. Xie, and A. H. MacDonald, Exact diagonalization for magic-angle twisted bilayer graphene, *Phys. Rev. Lett.* **127**, 147203 (2021).
- [30] J. S. Hofmann, E. Khalaf, A. Vishwanath, E. Berg, and J. Y. Lee, Fermionic monte carlo study of a realistic model of twisted bilayer graphene, *Phys. Rev. X* **12**, 011061 (2022).
- [31] X. Zhang, G. Pan, Y. Zhang, J. Kang, and Z. Y. Meng, Momentum space quantum monte carlo on twisted bilayer graphene, *Chinese Physics Letters* **38**, 077305 (2021).
- [32] Y. Da Liao, J. Kang, C. N. Breiør, X. Y. Xu, H.-Q. Wu, B. M. Andersen, R. M. Fernandes, and Z. Y. Meng, Correlation-induced insulating topological phases at charge neutrality in twisted bilayer graphene, *Phys. Rev. X* **11**, 011014 (2021).
- [33] C. Huang, X. Zhang, G. Pan, H. Li, K. Sun, X. Dai, and Z. Y. Meng, Evolution from quantum anomalous hall insulator to heavy-fermion semimetal in magic-angle twisted bilayer graphene, *Phys. Rev. B* **109**, 125404 (2024).
- [34] T. Soejima, D. E. Parker, N. Bultinck, J. Hauschild, and M. P. Zaletel, Efficient simulation of moiré materials using the density matrix renormalization group, *Phys. Rev. B* **102**, 205111 (2020).
- [35] S. Chatterjee, M. Ippoliti, and M. P. Zaletel, Skyrmion superconductivity: Dmrg evidence for a topological route to superconductivity, *Phys. Rev. B* **106**, 035421 (2022).
- [36] D. E. Parker, T. Soejima, J. Hauschild, M. P. Zaletel, and N. Bultinck, Strain-induced quantum phase transitions in magic-angle graphene, *Phys. Rev. Lett.* **127**, 027601 (2021).
- [37] T. Wang, D. E. Parker, T. Soejima, J. Hauschild, S. Anand, N. Bultinck, and M. P. Zaletel, Kekulé spiral order in magic-angle graphene: a density matrix renormalization group study (2022), arXiv:2211.02693 [cond-mat.str-el].
- [38] F. M. Faulstich, K. D. Stubbs, Q. Zhu, T. Soejima, R. Dilip, H. Zhai, R. Kim, M. P. Zaletel, G. K.-L. Chan, and L. Lin, Interacting models for twisted bilayer graphene: a quantum chemistry approach (2022), arXiv:2211.09243 [cond-mat.str-el].
- [39] H. Polshyn, M. Yankowitz, S. Chen, Y. Zhang, K. Watanabe, T. Taniguchi, C. R. Dean, and A. F. Young, Large linear-in-temperature resistivity in twisted bilayer graphene, *Nature Physics* **15**, 1011 (2019).
- [40] X. Lu, P. Stepanov, W. Yang, M. Xie, M. A. Aamir, I. Das, C. Urgell, K. Watanabe, T. Taniguchi, G. Zhang, A. Bachtold, A. H. MacDonald, and D. K. Efetov, Superconductors, orbital magnets and correlated states in magic-angle bilayer graphene, *Nature* **574**, 653 (2019).
- [41] Y. Saito, J. Ge, K. Watanabe, T. Taniguchi, and A. F. Young, Independent superconductors and correlated insulators in twisted bilayer graphene, *Nature Physics* **16**, 926 (2020).
- [42] P. Stepanov, I. Das, X. Lu, A. Fahimniya, K. Watanabe, T. Taniguchi, F. H. L. Koppens, J. Lischner, L. Levitov, and D. K. Efetov, Untying the insulating and superconducting orders in magic-angle graphene, *Nature* **583**, 375 (2020).
- [43] Y. Saito, J. Ge, L. Rademaker, K. Watanabe, T. Taniguchi, D. A. Abanin, and A. F. Young, Hofstadter subband ferromagnetism and symmetry-broken chern insulators in twisted bilayer graphene, *Nature Physics* **17**, 478 (2021).
- [44] S. Zhang and H. Krakauer, Quantum monte carlo method using phase-free random walks with slater determinants, *Phys. Rev. Lett.* **90**, 136401 (2003).
- [45] S. Zhang, J. Carlson, and J. E. Gubernatis, Constrained path monte carlo method for fermion ground states, *Phys. Rev. B* **55**, 7464 (1997).
- [46] S. Zhang, Auxiliary-field quantum monte carlo at zero- and finite-temperature, in *Many-Body Methods for Real Materials*, edited by E. Erik Koch and Shiwei Zhang (eds.) (Verlag des Forschungszentrum Jülich, 2019).
- [47] M. Suewattana, W. Purwanto, S. Zhang, H. Krakauer, and E. J. Walter, Phaseless auxiliary-field quantum monte carlo calculations with plane waves and pseudopo-

- tentials: Applications to atoms and molecules, *Phys. Rev. B* **75**, 245123 (2007).
- [48] W. Purwanto, H. Krakauer, Y. Virgus, and S. Zhang, Assessing weak hydrogen binding on Ca+ centers: An accurate many-body study with large basis sets, *The Journal of Chemical Physics* **135**, 164105 (2011), https://pubs.aip.org/aip/jcp/article-pdf/doi/10.1063/1.3654002/15444035/164105_1_online.pdf.
- [49] H. Shi and S. Zhang, Some recent developments in auxiliary-field quantum monte carlo for real materials, *The Journal of Chemical Physics* **154**, 024107 (2021), <https://doi.org/10.1063/5.0031024>.
- [50] J. Lee, H. Q. Pham, and D. R. Reichman, Twenty years of auxiliary-field quantum monte carlo in quantum chemistry: An overview and assessment on main group chemistry and bond-breaking, *Journal of Chemical Theory and Computation* **18**, 7024 (2022), pMID: 36255074, <https://doi.org/10.1021/acs.jctc.2c00802>.
- [51] J. Shee, J. L. Weber, D. R. Reichman, R. A. Friesner, and S. Zhang, On the potentially transformative role of auxiliary-field quantum Monte Carlo in quantum chemistry: A highly accurate method for transition metals and beyond, *The Journal of Chemical Physics* **158**, 10.1063/5.0134009 (2023), 140901, https://pubs.aip.org/aip/jcp/article-pdf/doi/10.1063/5.0134009/16824716/140901_1_5.0134009.pdf.
- [52] M. Suzuki, Relationship between d-Dimensional Quantum Spin Systems and (d+1)-Dimensional Ising Systems: Equivalence, Critical Exponents and Systematic Approximants of the Partition Function and Spin Correlations, *Progress of Theoretical Physics* **56**, 1454 (1976), <https://academic.oup.com/ptp/article-pdf/56/5/1454/5264429/56-5-1454.pdf>.
- [53] H. F. Trotter, On the product of semi-groups of operators, *Proceedings of the American Mathematical Society* **10**, 545 (1959).
- [54] J. Hubbard, Calculation of partition functions, *Phys. Rev. Lett.* **3**, 77 (1959).
- [55] R. L. Stratonovich, On a Method of Calculating Quantum Distribution Functions, *Soviet Physics Doklady* **2**, 416 (1957).
- [56] K. T. Williams, Y. Yao, J. Li, L. Chen, H. Shi, M. Motta, C. Niu, U. Ray, S. Guo, R. J. Anderson, J. Li, L. N. Tran, C.-N. Yeh, B. Mussard, S. Sharma, F. Bruneval, M. van Schilfegaarde, G. H. Booth, G. K.-L. Chan, S. Zhang, E. Gull, D. Zgid, A. Millis, C. J. Umrigar, and L. K. Wagner (Simons Collaboration on the Many-Electron Problem), Direct comparison of many-body methods for realistic electronic hamiltonians, *Phys. Rev. X* **10**, 011041 (2020).
- [57] M. Motta, C. Genovese, F. Ma, Z.-H. Cui, R. Sawaya, G. K. Chan, N. Chepiga, P. Helms, C. Jimenez-Hoyos, A. J. Millis, et al., Ground-state properties of the hydrogen chain: insulator-to-metal transition, dimerization, and magnetic phases, arXiv preprint arXiv:1911.01618 (2019).
- [58] J. P. F. LeBlanc, A. E. Antipov, F. Becca, I. W. Bulik, G. K.-L. Chan, C.-M. Chung, Y. Deng, M. Ferrero, T. M. Henderson, C. A. Jiménez-Hoyos, E. Kozik, X.-W. Liu, A. J. Millis, N. V. Prokof'ev, M. Qin, G. E. Scuseria, H. Shi, B. V. Svistunov, L. F. Tocchio, I. S. Tupitsyn, S. R. White, S. Zhang, B.-X. Zheng, Z. Zhu, and E. Gull (Simons Collaboration on the Many-Electron Problem), Solutions of the two-dimensional hubbard model: Benchmarks and results from a wide range of numerical algorithms, *Phys. Rev. X* **5**, 041041 (2015).
- [59] J. Carlson, J. E. Gubernatis, G. Ortiz, and S. Zhang, Issues and observations on applications of the constrained-path monte carlo method to many-fermion systems, *Phys. Rev. B* **59**, 12788 (1999).
- [60] Z.-Y. Xiao, H. Shi, and S. Zhang, Interfacing branching random walks with metropolis sampling: Constraint release in auxiliary-field quantum monte carlo, *Journal of Chemical Theory and Computation* **19**, 6782 (2023), pMID: 37661928, <https://doi.org/10.1021/acs.jctc.3c00521>.
- [61] M. Motta and S. Zhang, Computation of ground-state properties in molecular systems: Back-propagation with auxiliary-field quantum monte carlo, *Journal of Chemical Theory and Computation* **13**, 5367 (2017), pMID: 29053270, <https://doi.org/10.1021/acs.jctc.7b00730>.
- [62] H. Xu, H. Shi, E. Vitali, M. Qin, and S. Zhang, Stripes and spin-density waves in the doped two-dimensional hubbard model: Ground state phase diagram, *Phys. Rev. Res.* **4**, 013239 (2022).
- [63] M. Qin, C.-M. Chung, H. Shi, E. Vitali, C. Hubig, U. Schollwöck, S. R. White, and S. Zhang (Simons Collaboration on the Many-Electron Problem), Absence of superconductivity in the pure two-dimensional hubbard model, *Phys. Rev. X* **10**, 031016 (2020).
- [64] A. Blason and M. Fabrizio, Local kekulé distortion turns twisted bilayer graphene into topological mott insulators and superconductors, *Phys. Rev. B* **106**, 235112 (2022).
- [65] M. Angeli, E. Tosatti, and M. Fabrizio, Valley jahn-teller effect in twisted bilayer graphene, *Phys. Rev. X* **9**, 041010 (2019).

VII. IBM MODEL

A. BM model

We recap key features of the BM model [3, 30]. To establish a tight-binding description of TBG, we first consider electrons on two graphene layers with no inter-layer interactions (i.e., the distance between two layers $a_0 \rightarrow \infty$). We use unit cell index l , sub-lattice σ , and layer μ to identify the position of a selected carbon atom. We use $c_{l,m,s}^\dagger$, where $m = (\sigma, \mu)$, to specify the operator that creates an electron with spin s in the $2p_z$ orbital $\phi(\mathbf{r} - \mathbf{R}_{l,m})$ around the carbon atom at $\mathbf{R}_{l,m}$.

The Bloch state

$$\Phi_{\mathbf{p},m}(\mathbf{r}) = e^{i\mathbf{p}\cdot\mathbf{r}} u_{\mathbf{p},m}(\mathbf{r}) \quad (11)$$

where $u_{\mathbf{p},m}(\mathbf{r}) = u_{\mathbf{p},m}(\mathbf{r} + \mathbf{R}_{l,m})$ is a periodic function, under tight-binding approximation, can be written as:

$$\Phi_{\mathbf{p},m}(\mathbf{r}) = \sum_l e^{i\mathbf{p}\cdot\mathbf{R}_{l,m}} \phi(\mathbf{r} - \mathbf{R}_{l,m}).$$

In this appendix, $c_{\mathbf{p},m,s}^\dagger$ indicates creating a spin s electron with Bloch state $\Phi_{\mathbf{p},m}(\mathbf{r})$.

As demonstrated in Fig. 9, if two layers stack with a twisted angle θ , the Brillouin zones (BZ) of one monolayer of graphene rotate with angle θ relative to the other

layer, and this rotation leads to a periodic moire pattern and a mini-BZ (MBZ). With the above notations, the tight binding Hamiltonian of bilayer graphene with no inter-layer hopping (for \mathbf{p} measured around and from K_{\pm}^{μ} points) can be written as below:

$$\hat{H} = \sum_{\mathbf{p}} c_{\mathbf{p}}^{\dagger} T_{\mathbf{p},\mathbf{p}}^{\text{inter}} c_{\mathbf{p}} \quad (12)$$

$$T_{\mathbf{p},\mathbf{p}}^{\text{intra}} = \hbar v_F (p_x \sigma_x \tau_z + p_y \sigma_y) e^{-i\theta \sigma_z \mu_z \tau_z / 2},$$

where ν_F is Dirac velocity, $c_{\mathbf{p}}^{\dagger} = (\dots, c_{\mathbf{p},m,s}^{\dagger}, \dots)$ is a row vector of electron creation operators. $\mathbf{p} = (p_x, p_y)$ run over the 1st BZ of graphene at layer μ and the choice of the K_{\pm}^{μ} point is denoted by valley τ . τ_* , σ_* , and μ_* are the Pauli matrices for the related flavors.

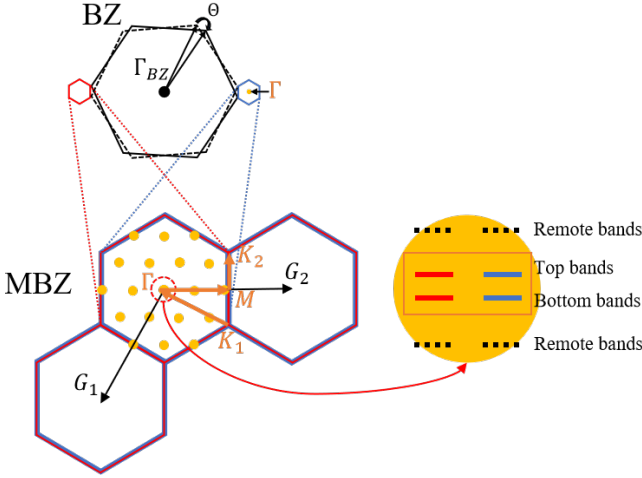


FIG. 9. Two twisted graphene Brillouin zones (BZ) with twisted angle θ and the corresponding mini Brillouin zones (MBZ) for TBG moire lattice generated from the twist. The momentum space hexagonal lattice (i.e., yellow point) discretizes MBZ. G_1 and G_2 are primitive vectors of the MBZ.

By incorporating inter-layer hopping into the tight-binding Hamiltonian and a $U_g = e^{-i\theta \sigma_z \mu_z \tau_z / 4}$ basis transformation (i.e., $c_{\mathbf{p}} \rightarrow U_g c_{\mathbf{p}}$), we have:

$$\hat{H}_{BM} = \sum_{\mathbf{p}} T_{\mathbf{p},\mathbf{p}}^{\text{intra}} c_{\mathbf{p}}^{\dagger} c_{\mathbf{p}} + T_{\mathbf{p}',\mathbf{p}}^{\text{inter}} c_{\mathbf{p}'}^{\dagger} c_{\mathbf{p}}$$

$$T_{\mathbf{p},\mathbf{p}}^{\text{intra}} = \hbar v_F (p_x \sigma_x \tau_z + p_y \sigma_y)$$

$$T_{\mathbf{p}',\mathbf{p}}^{\text{inter}} = \frac{1}{2} \sum_{l=0,1,2} \delta_{\mathbf{p}',\mathbf{p}-\tau_z \mathbf{q}_l} (\mu_x - i\mu_y) T_l + \text{h.c.}$$

$$T_l = \omega_0 e^{-i\theta \sigma_z \mu_z \tau_z / 2} + \omega_1 e^{2\pi i l \sigma_z \tau_z / 3} \sigma_x e^{-2\pi i l \sigma_z \tau_z / 3}, \quad (13)$$

where $\theta = 1.05^\circ$ is the twist angle, $\nu_F = 2700 * \frac{3a_0}{2\hbar}$ meV is the Dirac velocity, and ω_0, ω_1 describes lattice relaxation between A-A and A-B stacks, respectively. In this work, we take $\omega_1 = 105\text{meV}$ and tune $\kappa = \frac{\omega_0}{\omega_1}$ to scan ω_0 . Transition momentum $\mathbf{q}_l = R(2\pi l/3) \mathbf{q}_0$, where $R(\psi) = e^{i\psi \sigma_y}$ is a rotation matrix. $\mathbf{q}_0 = \frac{8\pi \sin(\theta/2)}{3\sqrt{3}a_0} (0, -1)^T$ and

$a_0 = 1.42\text{\AA}$ is the intra-layer distance between carbon atoms.

Since the model \hat{H}_{BM} [3] above are described in “microscopic basis” (i.e., unit cell index l , sub-lattice σ and layer μ), we transform it to “band basis” that simplifies the implementation of AFQMC. As demonstrated in Fig. 9, we discretize MBZ at valley τ as $L \times L$ lattice, and each lattice point is labeled by $\mathbf{k} + \mathbf{G} = (k_1 + m_1 * G_1, k_2 + m_2 * G_2)$ with \mathbf{k} running over the 1st MBZ and G_1, G_2 are the primitive vectors of MBZ. Γ point of the hexagon is set to be the origin $\mathbf{k} = (0, 0)$. We shift \mathbf{p} with $\mathbf{p} + K_{\pm}^{\mu} = \mathbf{k} + \mathbf{G} + \Gamma$, then \hat{H}_{BM} is block-diagonalized for \mathbf{k} , spin s , valley τ where only terms that connect \mathbf{k} and $\mathbf{k} + \mathbf{G}$ are non-zero. In the numerical study, we truncate \mathbf{G} with the closest N_G vectors ($-4 \leq m_1, m_2 \leq 4$ in this work). Then we can use $\varepsilon_{\mathbf{k},i}$ and $|\varphi_{\mathbf{k},i}\rangle$ to specify eigenvalues and eigenstates of each band $n = 0, \dots, N_G - 1$ in this model:

$$\hat{H}_{BM} |\varphi_{\mathbf{k},i}\rangle = \varepsilon_{\mathbf{k},i} |\varphi_{\mathbf{k},i}\rangle \quad (14)$$

which is in band basis labeled by $i = (s, \tau, n)$ and Bloch wave functions $|\varphi_{\mathbf{k},i}\rangle = \sum_{\mathbf{G},m} \alpha_{\mathbf{k}+\mathbf{G},i,m} |\Phi_{\mathbf{k}+\mathbf{G},m}\rangle$.

We limit this model to two flat bands closest to the Fermi level to allow a practical numerical study. We only consider one-body and two-body terms involving two flat bands $n = \pm$ where \pm specify the top and bottom flat bands. When $|\varphi_{\mathbf{k},i}\rangle$ are degenerated, we fix the gauge with C_2T symmetry as used in previous DQMC work [30].

B. Interacting BM model

The two-body interaction is already included in the BM model at an independent-electron level through the original ab initio density-functional computations. To include the screened Coulomb interaction, the IBM model in Eq. (3) also needs to include a background subtraction to correct this double-counting effect. The Coulomb interaction \hat{V} is limited in two flat bands, and the charge-density operators are shifted according to the chemical potential at n_f filling:

$$\bar{\rho}_{\mathbf{q}} = \sum_{\mathbf{k},i,j} d_{\mathbf{k}+\mathbf{q},i}^{\dagger} \Lambda(\mathbf{k} + \mathbf{q}, \mathbf{k})_{i,j} d_{\mathbf{k},j} - \frac{n_f}{8} \sum_{\mathbf{k}} \delta_{\mathbf{q},\mathbf{G}} \text{tr}\{\Lambda(\mathbf{k} + \mathbf{q}, \mathbf{k})\}$$

$$\Lambda(\mathbf{k} + \mathbf{q}, \mathbf{k})_{i,j} \equiv \sum_m \alpha_{\mathbf{k}+\mathbf{q},i,m}^* \alpha_{\mathbf{k},j,m} \quad (15)$$

where $d_{\mathbf{k},i}^{\dagger}$ create state $|\varphi_{\mathbf{k},i}\rangle = \sum_{\mathbf{G},m} \alpha_{\mathbf{k}+\mathbf{G},i,m} |\Phi_{\mathbf{k}+\mathbf{G},m}\rangle$ and momentum \mathbf{k} that runs over MBZ. The transfer momentum \mathbf{q} remains unrestricted but is truncated for numerical implementation which is $(-3 * G_1, -3 * G_2) \leq \mathbf{q} \leq (3 * G_1, 3 * G_2)$ in this work. The potential

$$V_{\mathbf{q}} = \frac{e^2}{2\epsilon\epsilon_0 A} \frac{1 \tanh(|\mathbf{q}|d)}{|\mathbf{q}|} \quad (16)$$

is the Fourier-transformed two-gate screened Coulomb interaction. $A = N_M A_0$ is the total area of the system with $A_0 = \sqrt{2} a_M^2 / 2$, $a_M = \sqrt{3} a_0 / 2 \sin \frac{\theta}{2} = 13.4$ nm and N_M is the number of moire unit cells of this system. We chose a distance $d = 20$ nm between two layers and relative permittivity $\epsilon = 10$ (ϵ_0 is vacuum permittivity). We study the choice of relative permittivity in App. XI.

The inclusion of the Coulomb interaction in \hat{V} should be accompanied by a removal of the double-counting of Coulomb interacting in \hat{H}_{BM} , as discussed earlier. The ‘‘bare’’ dispersion in TBG without Coulomb interaction involved is approximated with

$$H_0 = \hat{H}_{BM} - [\hat{V}]_{\phi_{BM}} = \sum_{\mathbf{k}, i} \epsilon_{\mathbf{k}, i} c_{\mathbf{k}, i}^\dagger c_{\mathbf{k}, i} - \sum_{\mathbf{k}, i, j} [V]_{\mathbf{k}, i; \mathbf{k}, j} c_{\mathbf{k}, i}^\dagger c_{\mathbf{k}, j}. \quad (17)$$

with a mean-field approximation $[V]$ of the Coulomb interaction. The choice of mean-field state to estimate the double counting correction $[V]_{\mathbf{k}, i; \mathbf{k}, j}$ can be varied. This paper uses the ground state of H_{BM} at $n_f = 4$ as our mean-field reference state ϕ_{BM} . The discrepancies between bare dispersion H_0 and BM model H_{BM} along κ are presented in Fig. 1.

In practice, we first write \hat{H}_{BM} (Eq. 13) in ‘‘microscopic basis’’ where basis are labeled with spin s , valley τ , layer μ and sublattice σ . We then diagonalize \hat{H}_{BM} for flat bands closest to the fermi surface and identify two bands through energy. For two flat bands that are degenerated (i.e., $\epsilon_{\mathbf{k}} = 0$), we break the degeneracy with C_2T and ‘‘small angle approximation’’ [30] by taking their eigenvectors as our specified bands. We take the set of bands and related spin, valley, as our band basis (labeled by n, s, τ) where H_{BM} is diagonalized.

VIII. SYMMETRY IN IBM MODEL

According to a previous study [13, 14], at the spinless limit, the ground states of IBM (without double counting correction) at chiral and flat band limit are single determinants:

- (Chern number ± 2) fill two bands in the same Chern sector \rightarrow quantum anomalous Hall states (QAH $\sigma_z \tau_z$).
- (Chern number 0) fill as linear combinations of the two bands in both Chern sectors \rightarrow Valley Polarized states (VP τ_z), Valley Hall states (VH σ_z), T-symmetric Inter-valley-coherent states (T-IVC $\sigma_x \tau_{x,y}$) and Kramers inter-valley-coherent states (K-IVC $\sigma_y \tau_{x,y}$).

The limit away from flat band can be considered perturbatively as an emergence of dispersion term:

$$h(\mathbf{k}) = h_0(\mathbf{k}) \tau_z + h_x(\mathbf{k}) \sigma_x + h_y(\mathbf{k}) \sigma_y \tau_z$$

that tunnel between opposite Chern (sublattice) bands belonging to the same valley, and we have

- At $\kappa = 0$, QAH, VH, and K-IVC are exact ground states if there is no dispersion. If dispersion is non-zero, the perturbation of the dispersion indicates the candidates of ground state prefer QAH, VH, and K-IVC.
- At $\kappa > 0$, the combination of interaction terms (an extra sublattice exchange term should be considered when $\kappa > 0$) and the perturbation of the dispersion prefer K-IVC.

HF [13, 26, 28] can produce the above correlated insulating states respectively by imposing corresponding symmetry breaking in the initial density. If the dispersion term is small, the breaking of $U_V(1)$ valley charge conservation indicates K-IVC state and the unbroken of $U_V(1)$ valley charge conservation (no inter-valley terms) combined with C_2T symmetry helps us to distinguish VH and QAH (C_2T symmetry is broken) with VP and SP state (C_2T symmetry is preserved). However, for a non-zero dispersion term, especially when perturbation fails, the solution of HF has no need to be eigenstates of QAH, VH, K-IVC correlation (i.e., exactly VH, QAH, and K-IVC state at flat band limit). In this paper, the term ‘‘K-IVC state’’ specifies HF ground state that have non-zero IVC, and ‘‘ C_2T -symmetry-breaking state’’ summarize all HF ground states that have no IVC and breaks C_2T symmetry (i.e., QAH and VH) as our study does not distinguish VH and QAH.

IX. LOW-LYING STATES AROUND CHIRAL LIMIT FOR $n_f = 4, 2$ FILLINGS

A. Spin gaps

We take the chiral limit for $n_f = 4, 2$ fillings. To determine the spin polarization, we calculate the spin gaps

$$\Delta_s = E(N_\uparrow - \delta N, N_\downarrow + \delta N) - E(N_\uparrow, N_\downarrow), \quad (18)$$

where $\delta N = 1, 2, \dots$. In Fig. 10, we show the spin gaps as a function of spin flips (δN) at $\kappa = 0.0$ from both HF and AFQMC. The reference states, with zero spin-flip, are the states with the lowest HF energy, namely, the non-spin polarized ground state ($N_\uparrow = N_\downarrow = N/2$) at $n_f = 4$ and fully spin-polarized state ($N_\uparrow = N, N_\downarrow = 0$) for $n_f = 2$ fillings. The AFQMC calculations used the corresponding HF state as a trial wave function. We show results from several lattice sizes, up to 12×12 , to help gauge finite-size effects. Our data support a vanishing spin gap around zero spin-flip.

B. Constraint robustness and further correction with constraint release

Many studies [56–58] have shown that AFQMC can recover from a constraining trial wave function which is

incorrect. However there has been no previous application of AFQMC to the MATBG system. Here we illustrate how in the most ambiguous cases we can reduce the dependence on which low-lying states as the trial wave function by constraint release.

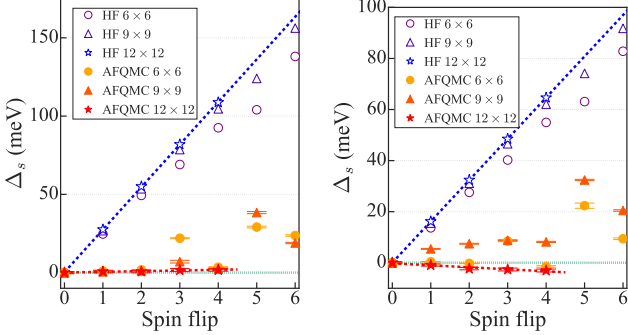


FIG. 10. Spin gap at the chiral limit ($\kappa = 0.0$) for fillings $n_f = 4$ (left panel) and $n_f = 2$ (right panel). Δ_s is shown as a function of δN for a small number of spin flips. States with zero spin-flip corresponds to the lowest HF energy. Dashed lines connect results from the largest lattice sizes 12×12 .

To distinguish low-lying states that are closely competing (i.e., K-IVC state and C_2T -symmetry-breaking state, which are degenerated at the chiral limit in the HF study), we detect ground state preference between these two states by comparing the energy difference between AFQMC with corresponding trial wave functions. That is the AFQMC run with lower energy gives a better description of the ground state. To resolve such a small difference, AFQMC with Metropolis release constraint [60] is performed to detect – and eliminate – any residual systematic bias from the constrained path approximation. AFQMC with Metropolis release can exponentially reduce the systematic bias by increasing released imaginary time β . In Fig. 12, we show the detailed convergence in energy for $\kappa = 0$. In Fig. 11, we summarise the comparison of converged energy in AFQMC with Metropolis release for different trial wave functions and different κ . We show that AFQMC with K-IVC trial wave function has lower energy for both $n_f = 4, 2$ fillings. Note that the competition between the ground states in K-IVC and C_2T -symmetry-breaking manifolds is only relevant when κ is small. The energy of ground states in K-IVC manifolds is much lower than the others for $\kappa \gg 0$.

X. ORDER PARAMETER

In AFQMC we can use the Hellman-Feynman theorem to calculate an order parameter $\langle \hat{O} \rangle$ by taking the derivative of energy over λ , [63]:

$$\langle \hat{O} \rangle = \lim_{\lambda \rightarrow 0} \frac{d \langle H_{IBM} + \lambda \hat{O} \rangle}{d\lambda}. \quad (19)$$

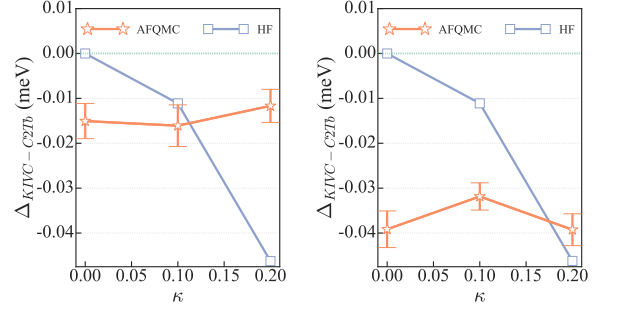


FIG. 11. Energy difference per electron between the ground states in K-IVC and C_2T -symmetry-breaking manifolds at different κ and 6×6 lattice for $n_f = 4$ fillings (left) and $n_f = 2$ fillings (right). AFQMC proceeds with the corresponding HF state as trial/initial wave functions. AFQMC with Metropolis release is performed to eliminate minor constraint bias.

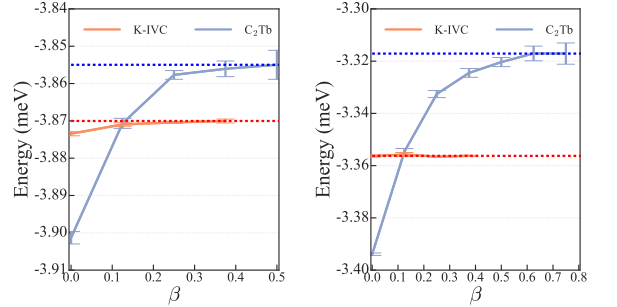


FIG. 12. Quantifying and reducing the constrained path error by AFQMC with Metropolis release constraint [60]. Energy per electron vs. released imaginary time β at $\kappa = 0$ for charge neutrality $n_f = 4$ (left) and half-filling $n_f = 2$ (right). Energy from AFQMC with K-IVC state or C_2T -symmetry-breaking state as the trial wave function is identified with orange and blue lines, respectively. Dashed lines indicate the converged energy for the Metropolis release procedure.

For a small range of λ around zero, we then use the numeric derivative of the energy to estimate the average of observables in the ground state.

In Fig. 13, we show more details about our calculations for K-IVC order parameter $\tau_x n_x$ and band occupancy n_z . To detect the K-IVC order, there is a two-fold degeneracy of the K-IVC pairs that favor $\tau_x n_x$ and $-\tau_x n_x$ (i.e., a direct estimation of $\tau_x n_x$ in the ground state without breaking the symmetry will always be zero). As presented in the top figures of Fig. 13, adding a positive λ will favor one of them to get lower energy and disfavor the other, which gives higher energy. We can produce a HF solution for one vs the other by imposing a corresponding initial density matrix. For $\kappa = 0$ (i.e., in the metallic phase), AFQMC with different HF trial wave functions gives similar energy with zero derivatives around $\lambda = 0$, supporting a loss of K-IVC order. As κ increases to the insulating phase, the linear behavior and the increase of derivatives in AFQMC indicate the appearance of K-IVC

order in the ground state. There is no such degeneracy in the calculation of band occupancy n_z , as the top and bottom bands have a non-zero gap. We observed a consistent linear behavior across $\lambda = 0$, and the derivatives decrease as κ increases, which indicates a reduction of the gap between the top and bottom band.

XI. THE CHOICE OF THE PERMITTIVITY ϵ

We explore the effects of the relative permittivity ϵ . In our study, we chose $\epsilon \approx 10$. To briefly verify the effects of different ϵ in determining the ground state, we present a direct comparison of two ϵ in terms of charge gap at $n_f = 2$ filling in Fig. XI. Our results show that by choosing a smaller $\epsilon = 5$, the charge gap is almost scaled by two, but the metal-insulator transition is still maintained.

These tests are obviously limited in scope and cannot rule out the possibility that some choice of ϵ might qualitatively change the ground state.

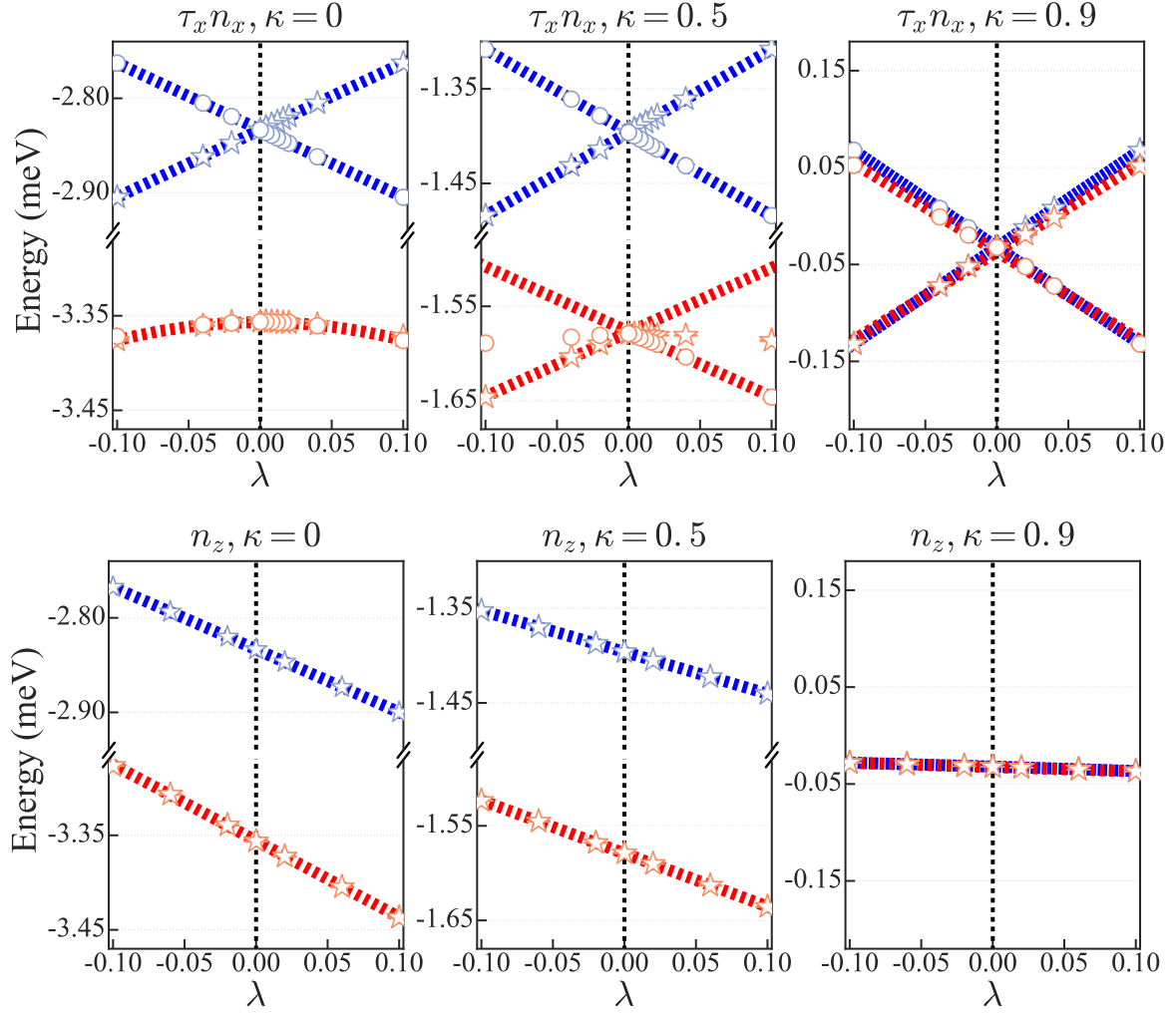


FIG. 13. Energy per electron versus λ for K-IVC order parameter $\tau_x n_x$ (top) and band occupancy n_z (bottom). HF results are presented in blue, while AFQMC results are highlighted in orange. Dashed lines/curves are linear/quadratic fitting to guide eyes. In the top figure, blue star and circle marks identify the energy of HF states that prefer $\tau_x n_x$ or $-\tau_x n_x$. The AFQMC results with corresponding HF states as trial wave functions are denoted by orange stars and circle marks. The derivative along λ indicates the preference of the corresponding order.

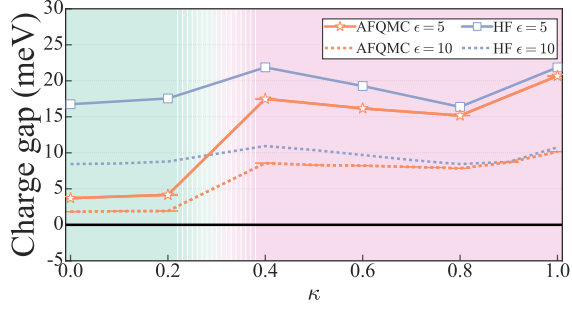


FIG. 14. Charge gap for $n_f = 2$ fillings versus κ for different choice of ϵ . Charge gaps are calculated by measuring the energy required to add or remove an electron from the system. AFQMC proceeds with the corresponding HF state as the trial wave function, the HF charge gap of which is illustrated in the figure. Shaded pink and green backgrounds separate the metallic/semi-metallic and insulating phases.